Journal of Energy Chemistry 90 (2024) 244–252

Contents lists available at ScienceDirect

Journal of Energy Chemistry

journal homepage: www.elsevier.com/locate/jechem

http://www.journals.elsevier.com/journal-of-energy-chemistry/

Valence electronic engineering of superhydrophilic Dy-evoked Ni-MOF outperforming RuO_2 for highly efficient electrocatalytic oxygen evolution

Zhiyang Huang [a], Miao Liao [a], Shifan Zhang [a], Lixia Wang [a], Mingcheng Gao [a], Zuyang Luo [a], Tayirjan Taylor Isimjan [c,*], Bao Wang [b,*], Xiulin Yang [a,*]

[a] Guangxi Key Laboratory of Low Carbon Energy Materials, School of Chemistry and Pharmaceutical Sciences, Guangxi Normal University, Guilin 541004, Guangxi, China
[b] State Key Laboratory of Biochemical Engineering, Institute of Process Engineering, Chinese Academy of Sciences, Beijing 100190, China
[c] Saudi Arabia Basic Industries Corporation (SABIC) at King Abdullah University of Science and Technology (KAUST), Thuwal 23955-6900, Saudi Arabia

ARTICLE INFO

Article history:
Received 5 September 2023
Revised 5 November 2023
Accepted 12 November 2023
Available online 22 November 2023

Keywords:
Dy@Ni-MOF
Dy incorporation
Electronic interaction
Superhydrophilicity
Oxygen evolution reaction

ABSTRACT

Tackling the problem of poor conductivity and catalytic stability of pristine metal-organic frameworks (MOFs) is crucial to improve their oxygen evolution reaction (OER) performance. Herein, we introduce a novel strategy of dysprosium (Dy) doping, using the unique 4*f* orbitals of this rare earth element to enhance electrocatalytic activity of MOFs. Our method involves constructing Dy-doped Ni-MOF (Dy@Ni-MOF) nanoneedles on carbon cloth via a Dy-induced valence electronic perturbation approach. Experiments and density functional theory (DFT) calculations reveal that Dy doping can effectively modify the electronic structure of the Ni active centers and foster a strong electronic interaction between Ni and Dy. The resulting benefits include a reduced work function and a closer proximity of the *d*-band center to the Fermi level, which is conducive to improving electrical conductivity and promoting the adsorption of oxygen-containing intermediates. Furthermore, the Dy@Ni-MOF achieves superhydrophilicity, ensuring effective electrolyte contact and thus accelerating reaction kinetics. Ex-situ and in-situ analysis results manifest Dy_2O_3/NiOOH as the actual active species. Therefore, Dy@Ni-MOF shows impressive OER performance, significantly surpassing Ni-MOF. Besides, the overall water splitting device with Dy@Ni-MOF as an anode delivers a low cell voltage of 1.51 V at 10 mA cm^{-2} and demonstrates long-term stability for 100 h, positioning it as a promising substitute for precious metal catalysts.

1. Introduction

Electrochemical water splitting, crucial in creating clean and renewable hydrogen (H_2), faces challenges due to the energy-intensive and sluggish kinetics of oxygen evolution reaction (OER) [1–3]. By designing efficient electrocatalysts, these issues can be significantly mitigated. Although noble metal-based catalysts, like IrO_2 and RuO_2, have been proven to be effective, their scarcity and high cost restrict their widespread application [4,5]. Therefore, it is necessary to explore more cost-effective alternatives, like non-noble metal-based OER catalysts.

A range of transition metal-based compounds including oxides, sulfides, phosphides, and metal-organic frameworks (MOFs) are now being investigated as potential OER electrocatalysts [6]. Thereinto, MOFs, crystalline porous materials formed by combining metal ions with organic linkers [7], offer the advantages of multiple active metal centers, adjustable microstructures, and controllable porous structures [8]. Yet, their application as efficient OER electrocatalysts is limited due to their poor electrical conductivity and stability [9,10]. Scientists have used methods like photo-induced lattice strain, pore-space-partition, heterointerface engineering, and heteroatom doping to overcome these limitations [11,12]. Notably, heteroatom doping has been proven to be effective in modifying the electronic structure of pristine MOFs, which enhances surface properties, facilitates charge transfer, and lowers the reaction energy barrier of the OER process, thereby boosting catalytic activity [13,14]. Incorporating a second metal into

* Corresponding authors.
E-mail addresses: isimjant@sabic.com (T.T. Isimjan), baowang@ipe.ac.cn (B. Wang), xlyang@gxnu.edu.cn (X. Yang).

https://doi.org/10.1016/j.jechem.2023.11.012

pristine MOFs can alter the electronic structure of the metal center, thus improving electrical conductivity [13]. In comparison to 3*d* orbitals of transition metals, the unique 4*f* orbitals of rare earth (RE) elements can overlap and hybridize with other orbitals, enabling them to act as electronic modulators, effectively regulating the electronic structure of catalysts. This modulation leads to a remarkable enhancement in the electrocatalytic properties and electrical conductivity of transition-metal-based catalysts [15–17]. Moreover, the coupling between *f*-*d* orbitals forms electronic ladders, which are advantageous for facilitating charge transfer and maintaining balanced intermediate adsorption energy [18,19]. Furthermore, the strong oxyphilic properties of RE elements enable flexible adjustment of oxygen electrocatalysis when incorporated into the material [20]. Simultaneously, RE elements are also considered promising dopants due to their capacity to reduce the electrical resistance of materials, resulting in increased electrical conductivity and enhanced electrocatalytic activity [21]. RE oxides typically act as a protective layer during electrocatalysis, offering corrosion resistance, which aids in bolstering catalyst stability [22]. Dysprosium (Dy), as an RE element with a +3 valence of $4f^9$, is a suitable dopant to address issues related to poor conductivity and stability in pristine MOFs, thereby leading to improved electrocatalytic activity [23,24]. Research also suggests that Dy and Ni spins exhibit ferromagnetic coupling, and Dy can influence the surface roughness of transition-metal-based catalysts [25,26]. Hence, doping RE elements into pristine MOFs is a viable electronic modulation strategy for enhancing the OER activity of catalysts.

Herein, we have incorporated dysprosium (Dy) into a nickel-based MOF (Ni-MOF), resulting in an effective OER catalyst. Experiments and density functional theory (DFT) calculations reveal that Dy doping not only ameliorates the surface properties of the Ni-MOF but also alters its electronic structure. Specifically, the addition of Dy endows the catalyst with superhydrophilic characteristics, enabling faster OER reaction kinetics. More importantly, Dy doping induces an intense Ni-Dy electronic interaction and optimizes the *d*-band center that facilitates the adsorption of oxygen-containing intermediates and reduces the reaction barrier. Additionally, Dy incorporation reduces the work function of the catalyst and brings the valence band closer to the Fermi level, thereby improving electrical conductivity. With these attributes, the obtained Dy@Ni-MOF presents outstanding OER performance. Remarkably, when used as the anode in a two-electrode electrolyzer, the cell voltage outperforms that of a conventional RuO_2 +-Pt/C assembled electrolyzer.

2. Experimental

2.1. Materials

Dysprosium nitrate hexahydrate ($Dy(NO_3)_3{\cdot}6H_2O$, 99.99%), 2, 5-dihydroxyterephthalic acid (DHTA, ≥98.0%), and salicylic acid (SA, 99.5%) were acquired from Shanghai Aladdin Biochemical Technology Co., Ltd. Nickel nitrate hexahydrate ($Ni(NO_3)_2{\cdot}6H_2O$, ≥98.0%), *N*, *N*-dimethylformamide (DMF, ≥99.5%), and ethanol (C_2H_5OH, ≥99.7%) were purchased from Xilong Science Co., Ltd. Potassium hydroxide (KOH, 90%) was bought from Shanghai Macklin Biochemical Technology Co., Ltd. Commercial Pt/C (20 wt% Pt) was obtained from Suzhou Sinero Technology Co., Ltd. Nafion solution (5 wt%) was obtained from Alfa Aesar. Carbon cloth (CC) was got from Kunshan Carbon Energy Technology Co., Ltd. RuO_2 powder was synthesized by direct calcination of $RuCl_3$ in air at 400 °C. All reagents and solvents were of analytical grade and could be used directly.

2.2. Synthesis of nanoneedle-shaped Dy@Ni-MOF on CC

Nanoneedle-shaped Dy@Ni-MOF was synthesized via a simple hydrothermal approach. Before synthesis, a piece of CC (1.5 cm × 3 cm) was ultrasonically cleaned in 0.5 M H_2SO_4, deionized (DI) water, and ethanol. Firstly, 0.1 mmol $Dy(NO_3)_3{\cdot}6H_2O$, 0.7 mmol $Ni(NO_3)_2{\cdot}6H_2O$, 0.216 mmol DHTA, and 0.216 mmol SA were added to the 18 mL mixed solution of DI water, ethanol, and DMF of 1:1:1 (*v*/*v*/*v*). After sonication treatment for 30 min, the solution and pretreated CC were transferred into a 30 mL Teflon-lined stainless steel autoclave and heated at 150 °C for 12 h. After natural cooling to room temperature, the sample was washed several times with DI water, and dried overnight at 50 °C. The synthesis of Ni-MOF or Dy_2O_3 on CC followed a process similar to that of Dy@Ni-MOF, with the exception that $Dy(NO_3)_3{\cdot}6H_2O$ or $Ni(NO_3)_2{\cdot}6H_2O$ was not added. Additionally, *x* Dy@Ni-MOF (*x* = 0.05, 0.1, and 0.2) was obtained by changing the amount of $Dy(NO_3)_3{\cdot}6H_2O$. Unless otherwise specified, the Dy@Ni-MOF represented 0.1 Dy@Ni-MOF.

2.3. Synthesis of RuO_2 and Pt/C on CC

1.9 mg RuO_2 or Pt/C was added to the 405 μL mixed solution (including 200 μL DI water, 200 μL ethanol, and 5 μL 5 wt% Nafion). The mixture was then ultrasonicated for 30 min to yield a homogeneous ink. Finally, the entire ink was pipetted onto the surface of the CC (1 cm × 1 cm) and dried naturally in the air. The mass loading of RuO_2 or Pt/C was approximately 1.9 mg cm^{-2}.

3. Results and discussion

3.1. Synthesis and structural analysis

Fig. 1(a) illustrates the preparation of Dy-doped Ni-based metal organic framework (Dy@Ni-MOF) nanoneedles grown on carbon cloth (CC) using a one-step hydrothermal method. Briefly, the inclusion of Dy^{3+} in a Ni^{2+}, DHTA, and SA mixture led to the formation of Dy@Ni-MOF. For comparison, a pristine Ni-MOF supported on CC was also synthesized. The structure of Dy@Ni-MOF was analyzed through X-ray powder diffraction (XRD). As depicted in Fig. 1 (b), the pristine Ni-MOF exhibits two primary diffraction peaks at roughly 6.8° and 11.8°, closely matching the theoretical simulations of Ni-MOF [27,28]. Besides, the broad peak near 25.8° can be assigned to the CC [29]. The Dy@Ni-MOF retains a similar crystal structure to the Ni-MOF after the Dy doping, demonstrating a low Dy-doping load. However, the main diffraction peaks of Dy@Ni-MOF perform a slight negative shift and decreased intensity compared to those of Ni-MOF, which can be attributed to the impact of Dy incorporation on the coordination between the original Ni center and the organic ligand, manifesting the successful incorporation of Dy into the Ni-MOF lattice [14]. Additionally, the XRD pattern indicates that the crystal surface diffraction peaks correspond to Dy_2O_3 (PDF#18-0475) when only monometallic Dy is present (Fig. S1), indicating that Dy atoms cannot actively coordinate with the ligands to form MOFs under the same preparation conditions. The characteristic peaks of Ni-MOF and Dy@Ni-MOF were further analyzed by Raman spectroscopy. As seen in Fig. 1(c), the peaks at 1321 and 1600 cm^{-1} are assigned to the D and G bands of the carbon cloth (CC), respectively [30]. The peaks at 1619, 1556, and 580 cm^{-1} correspond to the stretching and deformation vibrations of the benzene ring [31]. The minor peaks at 829 and 420 cm^{-1} are ascribed to the C–H bending mode of the benzene ring and the vibration of the metal–oxygen bond (Ni–O), respectively [28,32]. The COO^- vibration occurs at 1493 and 1419 cm^{-1}. The sharp peak at 1282 cm^{-1} is attributed to the C–O vibration, owing to the

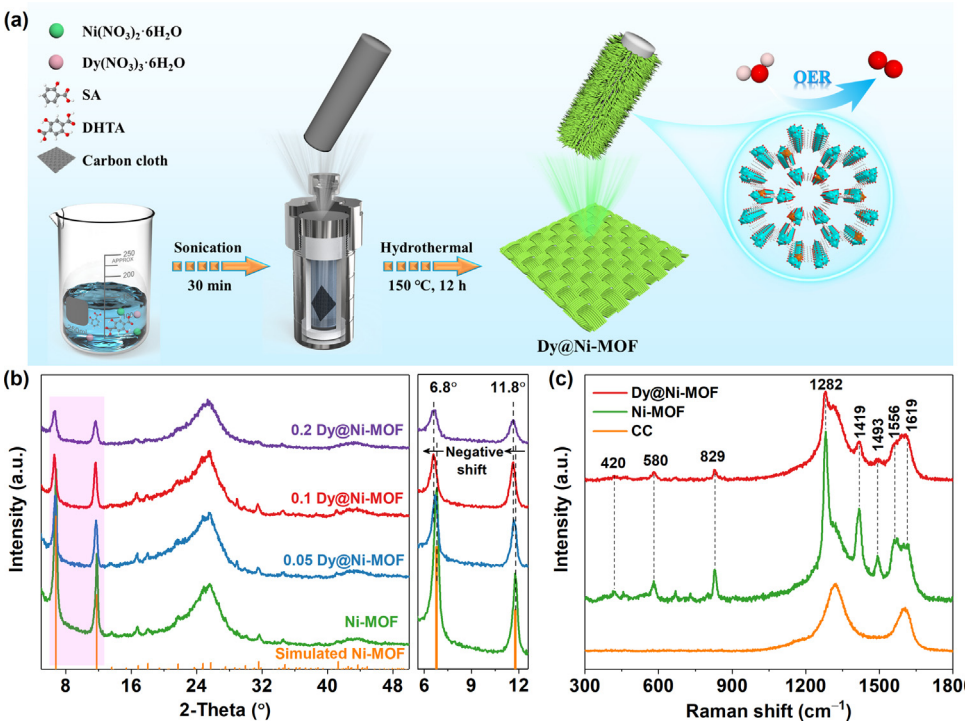

Fig. 1. (a) Schematic illustration for the formation of the Dy@Ni-MOF on carbon cloth. The cyan and orange balls in the structural model represent Ni and Dy atoms, respectively. (b) XRD patterns of Ni-MOF and (0.05, 0.1, and 0.2) Dy@Ni-MOF. (c) Raman spectra of carbon cloth, Ni-MOF, and Dy@Ni-MOF.

deprotonation of the hydroxyl group [33]. These results further validate the synthesis of the Ni-MOF. The surface functional groups in Ni-MOF and Dy@Ni-MOF were confirmed by Fourier transform infrared (FT-IR) spectroscopy (Fig. S2). Both Ni-MOF and Dy@Ni-MOF possess similar FT-IR spectra, revealing that their molecular structures are analogous [34]. The presence of COO^- vibration signals (1540 and 1388 cm^{-1}) verifies the existence of metal-organic coordination bonds, suggesting that some carboxylate groups are exposed on the Dy@Ni-MOF surface, which is beneficial for water adsorption during the OER process [35]. Additionally, the absence of the carboxylic group peak (1654 cm^{-1}) compared to the pure DHTA ligand confirms the lack of free ligand in Dy@Ni-MOF [35].

Scanning electron microscopy (SEM) and transmission electron microscopy (TEM) were employed to trace the morphology and microstructure of Ni-MOF and Dy@Ni-MOF. As demonstrated in Fig. 2(a) and Fig. S3(a), Ni-MOF displays a cotton-like morphology with significant agglomeration. Interestingly, after successful Dy doping, a series of Dy-doped Ni-MOF present a nanoneedle structure (Fig. 2b and Fig. S3b–d), suggesting that Dy incorporation significantly modifies the morphology of Ni-MOF and prevents material aggregation. When the doping amount is 0.1, the nanoneedles were grown uniformly on the carbon cloth, which promotes electrolyte dispersion and bubble release. The nanoneedle-shaped morphology of Dy@Ni-MOF is further confirmed by the TEM image (Fig. 2c). As shown in Fig. 2(d), there are no obvious lattice fringes in the high-resolution TEM (HR-TEM) image with ambiguous rings-like selected area electron diffraction (SAED) patterns of Dy@Ni-MOF. This observation may be attributed to the sensitivity of MOFs to high-energy electron beams, the buffering effect of hydrogen bonds, as well as the flexibility and relatively weak coordination between metal ions and ligands [36–38]. As viewed in Fig. 2(e and f), atomic force microscope (AFM) measurements also observe the nanoneedle morphology of Dy@Ni-MOF with an average thickness of about 137 nm. The high-angle annular dark-field scanning TEM (HAADF-STEM) and corresponding elemental mapping images reveal the even distribution of Ni, Dy, C, and O elements in Dy@Ni-MOF (Fig. 2g–k), which is a reliable evidence for the successful doping of Dy. According to the inductively coupled plasma mass spectrometry (ICP-MS), the Dy content in Dy@Ni-MOF is 2.55 wt% (Table S1).

X-ray photoelectron spectroscopy (XPS) was utilized to examine the elemental composition and surface chemical valence states of catalysts. As presented in Fig. S4(a), the XPS survey spectra reveal the existence of Ni, Dy, C, and O elements in Dy@Ni-MOF. The high-resolution C 1*s* spectrum (Fig. S4b) of Dy@Ni-MOF can be divided into C=C/C–C (284.0 eV), C=O (285.4 eV), and O–C=O (288.3 eV), respectively [27,34]. For the Ni 2*p* XPS core-level spectrum of Dy@Ni-MOF (Fig. 3a), the peaks at 856.1 and 873.8 eV are assigned to Ni^{2+} $2p_{3/2}$ and Ni^{2+} $2p_{1/2}$, respectively [39]. Notably, the observed shift of Ni 2*p* to higher binding energy in Dy@Ni-MOF compared to that of Ni-MOF implies that Dy can modulate the central electronic state of Ni, thereby forming high-valance Ni state and inducing an intense Ni-Dy electronic interaction, which is conducive to enhancing the OER activity [40,41]. This interaction favors adsorption of oxygen-containing intermediates and enhances OER activity [18]. The high-resolution Dy 4*d* spectrum (Fig. 3b) reveals two characteristic peaks at 153.8 and 156.9 eV, corresponding to the Dy $4d_{5/2}$ and Dy $4d_{3/2}$ of Dy^{3+} [23,42], which confirms the successful Dy doping in Ni-MOF. Besides, the deconvolution of the O 1*s* spectrum in Dy@Ni-MOF (Fig. 3c) discloses three peaks at 530.7, 531.5, and 532.7 eV corresponding to the metal–oxygen (M–O), O–C=O, and adsorbed H_2O molecules (H_2O_{ads}), respectively [43].

The electronic interaction between Ni and Dy in Dy@Ni-MOF was comprehensively analyzed through the valence electron structure of metal ions (Fig. S5) [44]. In the case of the Ni-O-Ni unit, the π-symmetry *d*-orbitals (t_{2g}) of Ni^{2+} are completely occupied, giving rise to a significant electron-electron (e^--e^-) repulsion interaction between the Ni^{2+} and bridging O^{2-} [45]. In contrast, the Ni-O-Dy unit, benefiting from the electronic configuration of Dy^{3+} [Xe] $4f^9$, features numerous unfilled 4*f* orbitals in Dy^{3+} that can act as electron acceptors. The interaction with the bridging O^{2-} via π-

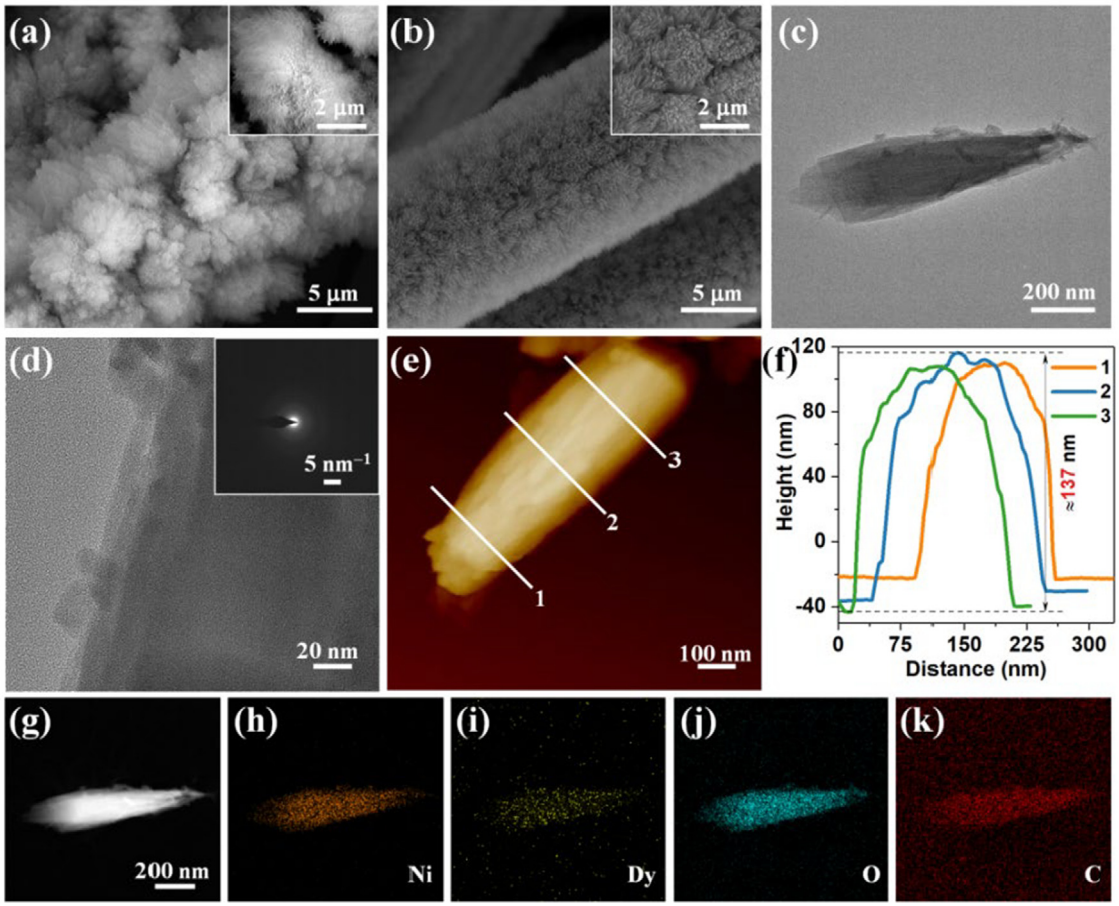

Fig. 2. SEM images of (a) Ni-MOF and (b) Dy@Ni-MOF. (c) TEM, (d) HR-TEM images (inset: the corresponding SAED pattern), (e) AFM image, (f) corresponding height profiles, (g) HAADF-STEM, and (h–k) corresponding elemental mapping images of Dy@Ni-MOF.

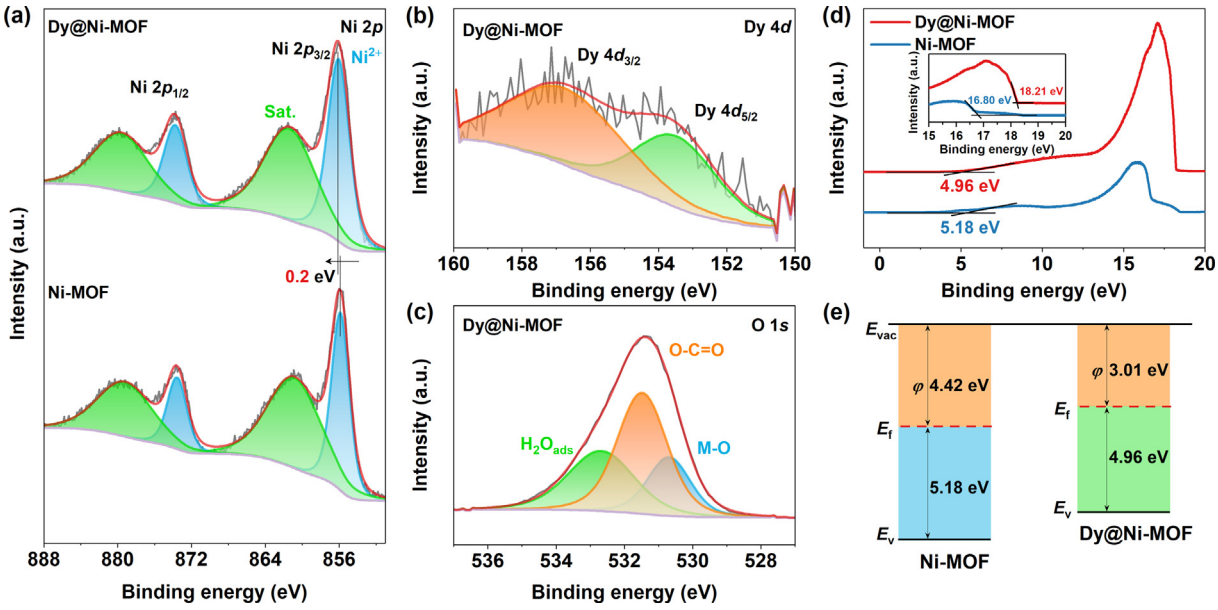

Fig. 3. High-resolution XPS survey spectra of (a) Ni 2*p* of Dy@Ni-MOF and Ni-MOF, (b) Dy 4*d* and (c) O 1*s* of Dy@Ni-MOF. (d) UPS spectra and (e) band structure alignment of Dy@Ni-MOF and Ni-MOF.

donation initiates the transfer of electrons from Ni^{2+} to Dy^{3+}, thereby converting Ni^{2+} ($t_{2g}^6e_g^2$) into the higher-valence Ni^{3+} ($t_{2g}^6e_g^1$), while simultaneously attenuating the e^--e^- repulsion with the bridging O^{2-} [46,47]. Consequently, Dy^{3+}, functioning as an electron acceptor, can extract electrons from the Ni sites through the Ni-O-Dy electronic coupling effect, ultimately leading to the

transformation of the Ni ions into a high-valence Ni state and the induction of a strong electron interaction between Ni and Dy.

Ultraviolet photoelectron spectroscopy (UPS) was applied to profoundly analyze the electronic property of Dy@Ni-MOF to further probe its enhanced intrinsic activity and fast kinetics. From Fig. 3(d and e), the work function (φ) values of Dy@Ni-MOF and Ni-MOF are calculated to be 3.01 and 4.42 eV, respectively. The decreased φ of Dy@Ni-MOF suggests that the doping of Dy makes it easier for electrons to be transferred from the interior of the catalyst to the surface to exchange electrons with reactants, thereby achieving quicker reaction kinetics [48]. In addition, the valence band maximum (E_v) values of Dy@Ni-MOF and Ni-MOF are found to be 4.96 and 5.18 eV, respectively. Obviously, the incorporation of Dy into Ni-MOF brings the valence band closer to the Fermi level (E_f), indicating better electrical conductivity of Dy@Ni-MOF [48,49].

3.2. OER performance in alkaline medium

The OER performance of the synthesized catalysts was tested in 1.0 M KOH. All potentials were 100% *iR* compensated and calibrated to the reversible hydrogen electrode (RHE) (Fig. S6). The optimum 0.1 Dy@Ni-MOF catalyst was obtained when the dosage of Dy was 0.1 mmol (Figs. S7 and S8). Henceforth, for simplicity, the 0.1 Dy@Ni-MOF will be referred to as Dy@Ni-MOF. Fig. 4(a) compares the linear sweep voltammetry (LSV) curves of Dy@Ni-MOF, Ni-MOF, and RuO_2, where Dy@Ni-MOF demonstrates notably enhanced OER activity compared to Ni-MOF. Furthermore, the superior catalytic activity of Dy@Ni-MOF compared to RuO_2 at current density exceeding 50 mA cm^{-2} can be attributed to its nanoneedles structure, which facilitates electrolyte diffusion and gas release [50]. Importantly, the oxidation peak of Ni^{2+} to Ni^{3+} is observed at approximately 0.10–0.17 V for Dy@Ni-MOF, demonstrating the surface reconstruction of MOFs into oxyhydroxides (e.g., NiOOH) [51]. The increased oxidation peak intensity of Dy@Ni-MOF manifests the presence of more active species to enhance OER activity [52]. To delve deeper into the OER kinetics, the corresponding Tafel slopes were derived from polarization curves (Fig. 4b). The Tafel slope value of Dy@Ni-MOF (96.5 mV dec^{-1}) is significantly lower than that of Ni-MOF (129.4 mV dec^{-1}) and comparable to that of RuO_2 (94.6 mV dec^{-1}), illustrating that Dy-introduction considerably accelerates OER kinetics. Additionally, the prominent OER performance of Dy@Ni-MOF surpasses most recently reported OER catalysts (Fig. 4c and Table S2). Electrochemical impedance spectroscopy (EIS) was employed to assess the charge-transfer capacity. As illustrated in Fig. 4(d), Dy@Ni-MOF possesses a lower charge transfer resistance (R_{ct} = 1.8 Ω) than Ni-MOF (R_{ct} = 5.1 Ω) and RuO_2 (R_{ct} = 3.1 Ω), demonstrating faster charge transfer and better electrical conductivity of Dy@Ni-MOF [53]. As depicted in Fig. S9, the synthesized Dy_2O_3 exhibits very poor OER performance, which is significantly inferior to that of Dy@Ni-MOF. Additionally, the turn frequency (TOF) was used to better understand the intrinsic OER activity (Fig. 4e). The TOF value (0.0168 s^{-1}) of Dy@Ni-MOF is significantly higher than that of Ni-MOF (0.0037 s^{-1}), attesting its splendid intrinsic OER activity. Noteworthily, the enhanced OER activity is not linked to the electrochemically active surface area (ECSA) [54,55]. As viewed in Fig. S10, the polarization curves normalized by ECSA further testify that the intrinsic activity of Dy@Ni-MOF immensely exceeds that of Ni-MOF. Therefore, these results certify that Dy doping plays a role in enhancing OER activity. In addition, the polarization curves show inappreciable changes after 1000 cycles (Fig. 4f), implying the extraordinary cycling stability of Dy@Ni-MOF. Simultaneously, Dy@Ni-MOF can operate continuously at a current density of 10 and 100 mA cm^{-2} for nearly 80 h without performance degradation (inset of Fig. 4f), proving its remarkable long-term stability.

3.3. Analyzing surface characteristics and active centers of Dy@Ni-MOF

To further confirm that the enhanced electrical conductivity of Dy@Ni-MOF is associated with Dy-doping, a digital multimeter

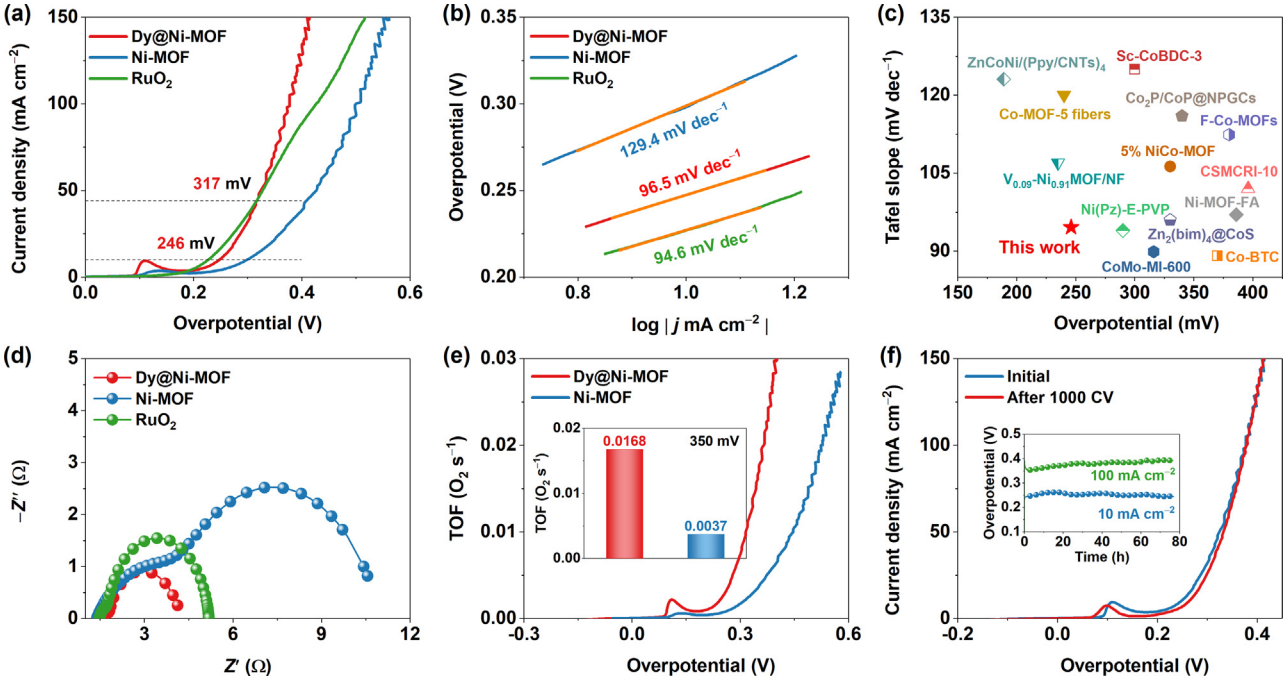

Fig. 4. OER activity of prepared catalysts in 1.0 M KOH solution. (a) LSV polarization curves. (b) Corresponding Tafel slopes. (c) Comparison of the overpotential at 10 mA cm^{-2} and Tafel slope with previously reported OER catalysts. (d) Electrochemical impedance spectroscopy. (e) Turnover frequency values. (f) Polarization curves of Dy@Ni-MOF before and after 1000 cycles (inset: chronopotentiometry of Dy@Ni-MOF at 10 and 100 mA cm^{-2}).

and a four-point probe were used to measure the material resistance and electrical conductivity, respectively. As shown in Fig. 5(a), the resistance of Dy@Ni-MOF is 37.90 Ω, significantly lower than that of Ni-MOF (169.09 Ω). Furthermore, Dy@Ni-MOF displays an electrical conductivity of 9.174 S cm^{-1} (Table S3), which is substantially higher than Ni-MOF (4.85 × 10^{-2} S cm^{-1}). These results testify that Dy doping can significantly improve the electrical conductivity, in agreement with the UPS and EIS analysis results discussed previously. Besides, the contact angle was measured to investigate the surface property changes after Dy doping in Ni-MOF. As displayed in Fig. 5(b), the contact angle decreases from 21° (Ni-MOF) to 0° (Dy@Ni-MOF), suggesting that the surface properties of Ni-MOF change after Dy incorporation, making Dy@Ni-MOF superhydrophilic. The superhydrophilicity facilitates tight contact between the electrolyte and the catalyst, thereby accelerating the reaction kinetics [56].

To further ascertain the practical active centers of Dy@Ni-MOF during the OER process, the microstructure, composition, and chemical state of Dy@Ni-MOF after OER test were investigated by SEM, XRD, TEM, XPS, and electrochemical in-situ Raman. As viewed in Figs. S11 and S12(a), the nanoneedle-shaped morphology of Dy@Ni-MOF remains essentially intact after OER test. Moreover, energy dispersive X-ray detector (EDX) elemental mappings disclose the uniform distribution of Ni, Dy, O, and C (Fig. S12b–e). The XRD results (Fig. S13) clearly demonstrate that Dy@Ni-MOF undergoes deep phase reconstruction after the OER test, resulting in the formation of low-crystallinity Dy_2O_3 and amorphous NiOOH. According to XPS analysis (Fig. S14), the peaks of Ni^{3+} at 857.3 and 875.4 eV emerge in the Ni 2*p* spectrum of Dy@Ni-MOF after OER test, which can be attributed to the generation of NiOOH, acting as active species [57]. Additionally, the characteristic peaks of Dy_2O_3 remain detectable in the Dy 4*d* high-resolution XPS spectrum of Dy@Ni-MOF after the OER test. Subsequently, electrochemical in-situ Raman spectroscopy was conducted to monitor the structural evolution of Dy@Ni-MOF during the OER (Fig. 5c and Fig. S15). As evident in Fig. 5(d), when the potential is maintained between 1.1 and 1.3 V (vs. RHE), the Raman spectra exclusively feature the characteristic peaks of MOFs. However, as the potential is raised, these MOF peaks progressively diminish. Notably, upon reaching 1.4 V (vs. RHE), the MOF characteristic peaks vanish, and two distinct peaks appear at 474 and 554 cm^{-1}, associated with the Ni–O vibration of NiOOH [51,52,58]. To further ascertain the conversion potential of NiOOH, the potential was adjusted between 1.3 and 1.4 V (vs. RHE) with an interval of 0.02 V. As seen in Fig. 5(e), Dy@Ni-MOF in situ transforms into the Dy@Ni-MOF/NiOOH complex at a potential of 1.36 V (vs. RHE), which generally aligns with the LSV curves. Ultimately, when the potential reaches 1.4 V (vs. RHE), the surface undergoes complete restructuring to Dy_2O_3/NiOOH. As a result, these findings conclusively indicate that Dy@Ni-MOF experiences surface reconstruction during the OER process, with the in-situ formed NiOOH serving as the actual active centers for OER (Fig. 5f).

3.4. OER mechanism investigation based on DFT calculations

DFT calculations were employed to investigate the impact of Dy doping on Dy@Ni-MOF during the OER process. Meanwhile, in order to make the theoretical simulation closer to the real catalyst surface, we considered the structural reconstruction. Therefore, based on the above ex-situ and in-situ analysis results, Dy_2O_3/NiOOH and NiOOH models with Ni sites as active sites were established and analyzed by DFT calculations (Fig. S16). The differential charge density maps (Fig. 6a and b) demonstrate that there is considerable charge accumulation at the interface of NiOOH and Dy_2O_3 whereas substantial electron depletion around Ni, suggesting the existence of strong electronic interactions between Ni and Dy species [7,59], which is in good agreement with the XPS results. The density of states (DOS) was calculated to gain further insight into the electronic structure changes of catalysts (Fig. 6c). For Dy_2O_3/NiOOH, there are ample DOS near the Fermi energy level (E_f), manifesting its higher electrical conductivity and faster charge transfer capability [7,13]. Moreover, the *d*-band center (ε_d) has

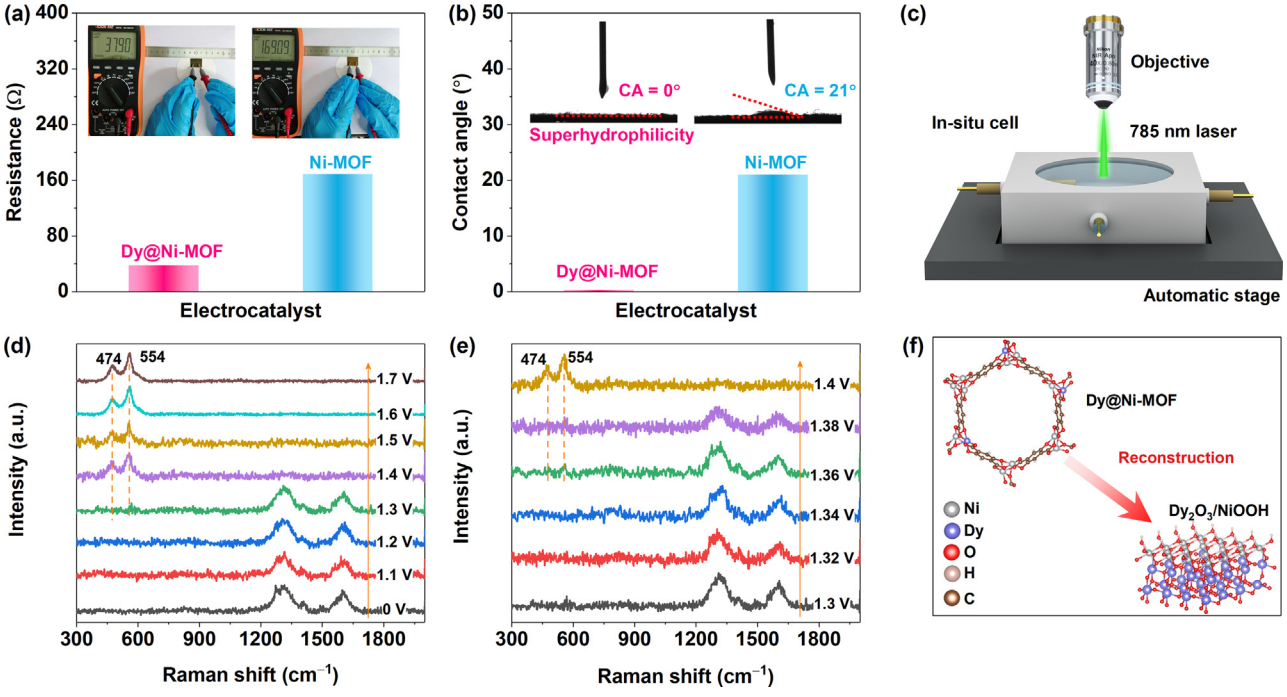

Fig. 5. (a) Photographs of Ni-MOF and Dy@Ni-MOF measuring resistance with a digital multimeter. (b) Contact angles of Ni-MOF and Dy@Ni-MOF. (c) Schematic diagram of electrochemical in-situ Raman cell. Electrochemical in-situ Raman spectra of (d) Dy@Ni-MOF at operating potentials from 1.1 to 1.7 V (vs. RHE) and (e) Dy@Ni-MOF at operating potentials from 1.3 to 1.4 V (vs. RHE). (f) Illustration of Dy@Ni-MOF reconstruction during OER reaction.

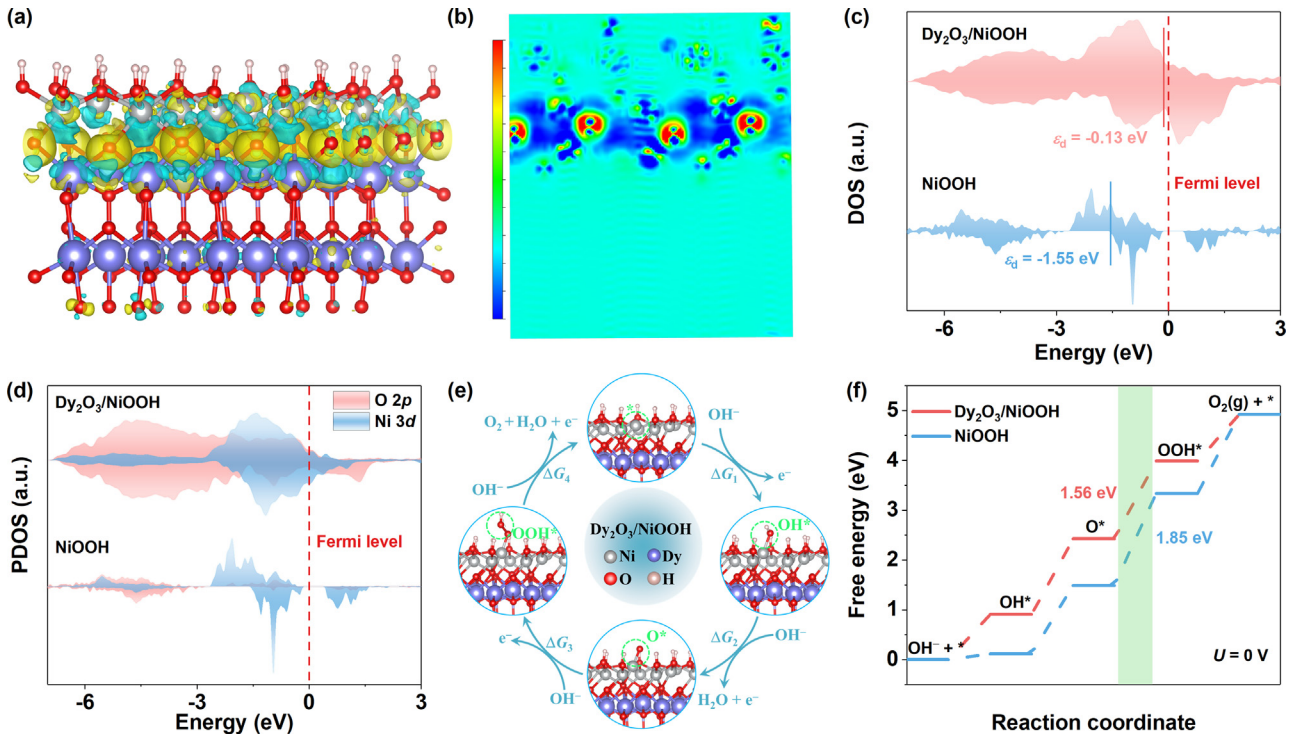

Fig. 6. DFT theoretical calculations. (a) The local structures and differential charge density and (b) two-dimensional (2D) charge density maps of Dy_2O_3/NiOOH. Yellow and cyan regions represent charge accumulation and depletion, respectively. (c) The calculated DOS and (d) PDOS of Ni 3*d* and O 2*p* for Dy_2O_3/NiOOH and NiOOH. (e) Schematic of the OER catalytic mechanism for Dy_2O_3/NiOOH. (f) OER Gibbs free energy diagrams for Dy_2O_3/NiOOH and NiOOH.

been recognized as a reliable indicator of the binding strength between catalysts and oxygen-containing intermediates (∗O, ∗OH, and ∗OOH), where the adsorption between catalysts and the oxygen-containing intermediates will be stronger when the ε_d approaches the E_f [60]. Remarkably, the ε_d value of Dy_2O_3/NiOOH (−0.13 eV) is higher than that of NiOOH (−1.55 eV). This indicates an upshift of ε_d energy levels and an elevation of antibonding energy states following Dy doping, which is conducive to enhancing the adsorption of oxygen-containing intermediates during the OER process [61]. Additionally, the calculated partial density of states (PDOS) demonstrates a robust orbital overlap between Ni and adsorbed oxygen intermediates in close proximity to the E_f (Fig. 6d), suggesting a strong electron coupling between Ni 3*d* orbitals in Dy_2O_3/NiOOH and O 2*p* orbitals of adsorbed oxygen intermediates [62].

The Gibbs free energy (ΔG) for each OER step is calculated based on the following four-electron transfer mechanism [63].

$$* + OH^- \rightarrow *OH + e^- \quad (1)$$

$$*OH + OH^- \rightarrow *O + H_2O + e^- \quad (2)$$

$$*O + OH^- \rightarrow *OOH + e^- \quad (3)$$

$$*OOH + OH^- \rightarrow * + O_2 + H_2O + e^- \quad (4)$$

where ∗ represents the active site and ∗O, ∗OH, and ∗OOH are the three oxygen-containing intermediates. Fig. 6(e) and Fig. S17 display the OER pathways and optimized OER intermediate adsorption configurations for Dy_2O_3/NiOOH and NiOOH, respectively. The optimized adsorbed molecules are all found on the Ni sites, indicating that Ni sites act as the primary active sites for the OER, which is in mutual agreement with the experimental results. To intuitively comprehend the OER reaction kinetics, the ΔG of each OER step was calculated without the additional potential (U = 0 V), where the step with the most significant change in ΔG is considered as the rate-determining step (RDS) [64]. As described in Fig. 6(f), the RDS for Dy_2O_3/NiOOH and NiOOH is the transformation of ∗O into ∗OOH [65], where the ΔG_3 value (1.56 eV) of Dy_2O_3/NiOOH is much lower than that of NiOOH (1.85 eV), indicating its faster OER kinetics [66]. Therefore, Dy doping can greatly optimize the electronic structure of the active Ni sites and produce a strong electron interaction, which is conducive to optimizing the adsorption of oxygen-containing intermediates and accelerating the OER kinetics, thereby enhancing OER activity.

3.5. Electrocatalytic performance for overall water splitting

Motivated by the exceptional OER performance of Dy@Ni-MOF, a two-electrode system was assembled with Pt/C and Dy@Ni-MOF as cathode and anode (labeled as Dy@Ni-MOF$^{(+)}$||Pt/C$^{(-)}$) to drive the overall water splitting (Fig. 7a). As shown in Fig. 7(b), Dy@Ni-MOF$^{(+)}$||Pt/C$^{(-)}$ displays splendid overall water splitting performance in 1.0 M KOH, which can deliver ultra-low cell voltages of 1.51 and 1.67 V at 10 and 100 mA cm^{-2}, respectively, outperforming commercial $RuO_2^{(+)}$||Pt/C$^{(-)}$. Moreover, the outstanding overall water splitting performance of Dy@Ni-MOF transcends most previously reported electrocatalysts (Fig. 7c and Table S4). More importantly, the overall water splitting activity of Dy@Ni-MOF can maintain stable for 100 h at 10 and 100 mA cm^{-2} (Fig. 7d), proving its excellent stability.

The excellent OER performance can be explained as follows reasons. Firstly, the introduction of Dy doping confers superhydrophilic properties to the catalyst, which is in favor of the intimate contact between the electrolyte and catalyst, thereby promoting the rapid penetration and mass transfer of electrolyte in the Dy@Ni-MOF catalyst [67,68]. Additionally, Dy doping into Ni-MOF causes electronic structure perturbation that contributes to optimizing the valence band and decreasing the work function,

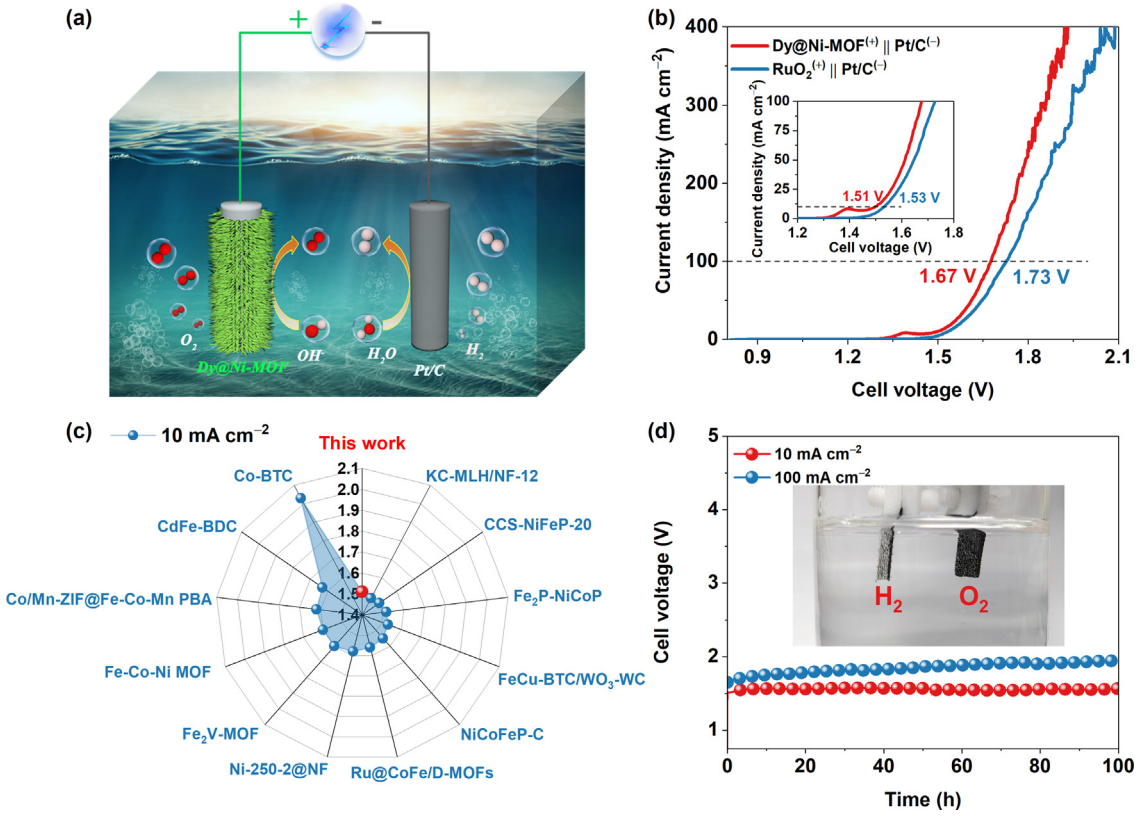

Fig. 7. (a) Schematic diagram of overall water splitting in a two-electrode system. (b) LSV curves of overall water splitting for Dy@Ni-MOF$^{(+)}$||Pt/C$^{(-)}$ and $RuO_2^{(+)}$||Pt/C$^{(-)}$ in 1.0 M KOH. (c) Comparison of the cell voltage of Dy@Ni-MOF at 10 mA cm^{-2} with recently reported catalysts. (d) Chronopotentiometry test at 10 and 100 mA cm^{-2}.

thus expediting electron transfer and improving electrical conductivity. More importantly, Dy incorporation leads to charge redistribution of Ni metal centers, creating strong 3*d*-4*f* orbital coupling effects, which can mediate the ionic and covalent competition of oxygen-containing intermediates to produce more up-shifted electronic states [20], thereby optimizing the adsorption of oxygen-containing intermediates and accelerating the proton-coupled electron transfer kinetics. Consequently, Dy as a dopant of transition metal MOF-based catalysts can induce valence electronic modulation and thus enhance OER activity.

4. Conclusions

In summary, we successfully fabricated rare-earth element Dy-doped Ni-MOF nanoneedles (Dy@Ni-MOF) on carbon cloth (CC) using a unique Dy-induced valence electronic perturbation method. The introduction of Dy substantially improves the surface properties of pristine Ni-MOF, making it superhydrophilic and thus achieving favorable electrolyte wettability. Additionally, Dy doping effectively modulates the electronic structure of the Ni active center, which not only induces an intense electronic interaction between Ni and Dy but also reduces the work function and valence band maximum, which is beneficial to expediting charge transfer and improving electrical conductivity. The in-situ/ex-situ techniques demonstrate that in-situ generated Dy_2O_3/NiOOH serves as the true active species during the OER process. The DFT calculations show that the introduction of Dy in Dy_2O_3/NiOOH shifts the center of the *d*-band center towards the Fermi level, which is favorable to enhance the adsorption of oxygen-containing intermediates and reduce the reaction energy barrier of RDS, thus improving the OER activity. As a result, the Dy@Ni-MOF presents eminent OER performance with a low overpotential (246 mV at 10 mA cm^{-2}) and small Tafel slope (94.6 mV dec^{-1}), superior to pristine Ni-MOF. Furthermore, the Dy@Ni-MOF$^{(+)}$||Pt/C$^{(-)}$ just requires an ultra-low cell voltage of 1.51 V to drive 10 mA cm^{-2}, outperforming the $RuO_2^{(+)}$||Pt/C$^{(-)}$. Meanwhile, the Dy@Ni-MOF-based electrolyzer also exhibits impressive stability during a 100 h durability test, implying its promising commercial application prospects. This work provides an effective strategy for incorporating rare-earth elements into pristine MOFs to develop high-performance and stable rare-earth-doped MOFs-based OER electrocatalysts.

Declaration of competing interest

The authors declare that they have no known competing financial interests or personal relationships that could have appeared to influence the work reported in this paper.

Acknowledgments

This work has been supported by the National Natural Science Foundation of China (52363028, 21965005), the Natural Science Foundation of Guangxi Province (2021GXNSFAA076001), and the Guangxi Technology Base and Talent Subject (GUIKE AD18126001, GUIKE AD20297039).

Appendix A. Supplementary data

Supplementary data to this article can be found online at https://doi.org/10.1016/j.jechem.2023.11.012.

References

[1] R. Mehmood, W. Fan, X. Hu, J. Li, P. Liu, Y. Zhang, Z. Zhou, J. Wang, M. Liu, F. Zhang, J. Am. Chem. Soc. 145 (2023) 12206–12213.
[2] Y.Z. Ke Sun, J. Yin, J. Jin, H. Liu, P. Xi, Acta Phys. Chim. Sin. 38 (2022) 2107005.
[3] S. Ren, X. Duan, S. Liang, M. Zhang, H. Zheng, J. Mater. Chem. A 8 (2020) 6144–6182.
[4] Q. Peng, Q. He, Y. Hu, T.T. Isimjan, R. Hou, X. Yang, J. Energy Chem. 65 (2022) 574–582.
[5] L.Z. Daqiang Yan, Z. Chen, W. Xiao, X. Yang, Acta Phys. Chim. Sin. 37 (2021) 2009054.
[6] Q. Zhang, H. Wang, W. Han, L. Yang, Y. Zhang, Z. Bai, Nano Res. 16 (2023) 3695–3702.
[7] J. Yang, Y. Shen, Y. Sun, J. Xian, Y. Long, G. Li, Angew. Chem. Int. Ed. 62 (2023) e202302220.
[8] S. Zhang, D. Lv, A. Zhou, D. Wang, D. Cai, J. Alloys Compd. 943 (2023) 169091.
[9] P. Zhou, J. Lv, X. Huang, Y. Lu, G. Wang, Coord. Chem. Rev. 478 (2023) 214969.
[10] Y. Peng, S. Sanati, A. Morsali, H. García, Angew. Chem. Int. Ed. 62 (2023) e202214707.
[11] C. Ni, H. Zheng, W. Liu, L. Wu, R. Li, K. Zhou, W. Zhang, Adv. Funct. Mater. 33 (2023) 2301075.
[12] Y. Kong, D. Xiong, C. Lu, J. Wang, T. Liu, S. Ying, X. Ma, F.-Y. Yi, ACS Appl. Mater. Interfaces 14 (2022) 37804–37813.
[13] J. Hu, Q. Xu, X. Wang, X. Huang, C. Zhou, Y. Ye, L. Zhang, H. Pang, Carbon Energy 5 (2023) e315.
[14] X. Zhang, X. Fang, K. Zhu, W. Yuan, T. Jiang, H. Xue, J. Tian, J. Power Sources 520 (2022) 230882.
[15] F. Tan, Y. Zhou, H. Zhang, P. Sun, H. Li, X. Liu, T. Wågberg, G. Hu, Chem. Eng. J. 454 (2023) 140079.
[16] F. Li, M. Jiang, C. Lai, H. Xu, K. Zhang, Z. Jin, Nano Lett. 22 (2022) 7238–7245.
[17] M. Li, Y. Wang, Y. Zheng, G. Fu, D. Sun, Y. Li, Y. Tang, T. Ma, Adv. Energy Mater. 10 (2020) 1903833.
[18] Y. Zhu, X. Wang, X. Zhu, Z. Wu, D. Zhao, F. Wang, D. Sun, Y. Tang, H. Li, G. Fu, Small 19 (2023) 2206531.
[19] X. Wang, J. Wang, P. Wang, L. Li, X. Zhang, D. Sun, Y. Li, Y. Tang, Y. Wang, G. Fu, Adv. Mater. 34 (2022) 2206540.
[20] C. Fan, X. Wang, X. Wu, Y. Chen, Z. Wang, M. Li, D. Sun, Y. Tang, G. Fu, Adv. Energy Mater. 13 (2023) 2203244.
[21] J.D. Rodney, S. Deepapriya, M.C. Robinson, C.J. Raj, S. Perumal, B.C. Kim, S. Krishnan, S.J. Das, Int. J. Hydrogen Energy 46 (2021) 27585–27596.
[22] X. Wang, Y. Tang, J.-M. Lee, G. Fu, Chem Catal. 2 (2022) 967–1008.
[23] Y. Ma, G.-M. Mu, Y.-J. Miao, D.-M. Lin, C.-G. Xu, F.-Y. Xie, W. Zeng, Rare Met. 41 (2022) 844–850.
[24] Z. Wan, Q. He, J. Chen, T.T. Isimjan, B. Wang, X. Yang, Chin. J. Catal. 41 (2020) 1745–1753.
[25] A. Okazawa, T. Nogami, H. Nojiri, T. Ishida, Inorg. Chem. 47 (2008) 9763–9765.
[26] X.T. Tang, Z.W. Lu, A.Z. Sun, J. Magn. Magn. Mater. 475 (2019) 10–13.
[27] P. Man, B. He, Q. Zhang, Z. Zhou, C. Li, Q. Li, L. Wei, Y. Yao, J. Mater. Chem. A 7 (2019) 27217–27224.
[28] H. Yu, L. Wang, H. Li, Z. Luo, T.T. Isimjan, X. Yang, Chem. Eur. J. 28 (2022) e202201784.
[29] Z. Huang, Z. Liu, M. Liao, L. Wang, Z. Luo, T.T. Isimjan, X. Yang, Chem. Eng. J. 462 (2023) 142281.
[30] Z. Liu, J. Wang, C. Zhan, J. Yu, Y. Cao, J. Tu, C. Shi, J. Mater. Sci. Technol. 46 (2020) 177–184.
[31] H. Seema, K.C. Kemp, S. Subhan, M. Yaseen, Int. J. Hydrogen Energy 47 (2022) 34762–34772.
[32] S. Naik Shreyanka, J. Theerthagiri, S.J. Lee, Y. Yu, M.Y. Choi, Chem. Eng. J. 446 (2022) 137045.
[33] Q. Wang, F. Wei, D. Manoj, Z. Zhang, J. Xiao, X. Zhao, F. Xiao, H. Wang, S. Wang, Chem. Commun. 55 (2019) 11307–11310.
[34] J. Xing, K. Guo, Z. Zou, M. Cai, J. Du, C. Xu, Chem. Commun. 54 (2018) 7046–7049.
[35] J. Zhou, Z. Han, X. Wang, H. Gai, Z. Chen, T. Guo, X. Hou, L. Xu, X. Hu, M. Huang, S.V. Levchenko, H. Jiang, Adv. Funct. Mater. 31 (2021) 2102066.
[36] W. Zheng, M. Liu, L.Y.S. Lee, ACS Catal. 10 (2020) 81–92.
[37] X. Gong, K. Gnanasekaran, Z. Chen, L. Robison, M.C. Wasson, K.C. Bentz, S.M. Cohen, O.K. Farha, N.C. Gianneschi, J. Am. Chem. Soc. 142 (2020) 17224–17235.
[38] Z.-X. Cai, Y. Xia, Y. Ito, M. Ohtani, H. Sakamoto, A. Ito, Y. Bai, Z.-L. Wang, Y. Yamauchi, T. Fujita, ACS Nano 16 (2022) 20851–20864.
[39] Z. Gao, Z.W. Yu, F.Q. Liu, Y. Yu, X.M. Su, L. Wang, Z.Z. Xu, Y.L. Yang, G.R. Wu, X.F. Feng, F. Luo, Inorg. Chem. 58 (2019) 11500–11507.
[40] T. Chen, F. Wang, S. Cao, Y. Bai, S. Zheng, W. Li, S. Zhang, S.-X. Hu, H. Pang, Adv. Mater. 34 (2022) 2201779.
[41] W. Cheng, X. Zhao, H. Su, F. Tang, W. Che, H. Zhang, Q. Liu, Nat. Energy 4 (2019) 115–122.
[42] R. Tholkappiyan, K. Vishista, Appl. Surf. Sci. 351 (2015) 1016–1024.
[43] Y. Luo, X. Yang, L. He, Y. Zheng, J. Pang, L. Wang, R. Jiang, J. Hou, X. Guo, L. Chen, ACS Appl. Mater. Interfaces 14 (2022) 46374–46385.
[44] J. Jiang, F. Sun, S. Zhou, W. Hu, H. Zhang, J. Dong, Z. Jiang, J. Zhao, J. Li, W. Yan, M. Wang, Nat. Commun. 9 (2018) 2885.
[45] S. Zhao, Y. Wang, J. Dong, C.-T. He, H. Yin, P. An, K. Zhao, X. Zhang, C. Gao, L. Zhang, J. Lv, J. Wang, J. Zhang, A.M. Khattak, N.A. Khan, Z. Wei, J. Zhang, S. Liu, H. Zhao, Z. Tang, Nat. Energy 1 (2016) 16184.
[46] X. Liu, S. Cao, J. Li, Y. Wang, W. Xue, G. Liu, Small (2023), https://doi.org/10.1002/smll.202304652.
[47] C.-F. Li, J.-W. Zhao, L.-J. Xie, J.-Q. Wu, Q. Ren, Y. Wang, G.-R. Li, Angew. Chem. Int. Ed. 60 (2021) 18129–18137.
[48] Y. Song, M. Sun, S. Zhang, X. Zhang, P. Yi, J. Liu, B. Huang, M. Huang, L. Zhang, Adv. Funct. Mater. 33 (2023) 2214081.
[49] J. Sun, L. Du, B. Sun, G. Han, Y. Ma, J. Wang, H. Huo, P. Zuo, C. Du, G. Yin, J. Energy Chem. 54 (2021) 217–224.
[50] M. Guo, A. Qayum, S. Dong, X. Jiao, D. Chen, T. Wang, J. Mater. Chem. A 8 (2020) 9239–9247.
[51] W. Wu, Z. Gao, Q. Li, Z. Wang, S. Liu, H. Wu, Y. Zhao, Y. Jiao, X. Zhao, J. Energy Chem. 74 (2022) 404–411.
[52] H. Sun, X. Xu, Z. Yan, X. Chen, F. Cheng, P.S. Weiss, J. Chen, Chem. Mater. 29 (2017) 8539–8547.
[53] Y. Bao, M. Zha, P. Sun, G. Hu, L. Feng, J. Energy Chem. 59 (2021) 748–754.
[54] N. Li, L. Cai, G. Gao, Y. Lin, C. Wang, H. Liu, Y. Liu, H. Duan, Q. Ji, W. Hu, H. Tan, Z. Qi, L.-W. Wang, W. Yan, Nano Lett. 22 (2022) 6988–6996.
[55] H.C. Fu, X.H. Wang, X.H. Chen, Q. Zhang, N.B. Li, H.Q. Luo, Appl. Catal. B Environ. 301 (2022) 120818.
[56] Z. Wu, Y. Zhao, H. Wu, Y. Gao, Z. Chen, W. Jin, J. Wang, T. Ma, L. Wang, Adv. Funct. Mater. 31 (2021) 2010437.
[57] W. He, R. Zhang, H. Liu, Q. Hao, Y. Li, X. Zheng, C. Liu, J. Zhang, H.L. Xin, Small 19 (2023) 2301610.
[58] Y. Shi, W. Du, W. Zhou, C. Wang, S. Lu, S. Lu, B. Zhang, Angew. Chem. Int. Ed. 59 (2020) 22470–22474.
[59] M. Guo, Z. Huang, Y. Qu, L. Wang, H. Li, T.T. Isimjan, X. Yang, Appl. Catal. B: Environ. 320 (2023) 121991.
[60] D. Liu, C. Wang, Z. Zhou, C. Ye, R. Yu, C. Wang, Y. Du, Inorg. Chem. Front. 9 (2022) 6158–6166.
[61] S. Sun, X. Zhou, B. Cong, W. Hong, G. Chen, ACS Catal. 10 (2020) 9086–9097.
[62] Y. Zhao, X.F. Lu, Z.-P. Wu, Z. Pei, D. Luan, X.W. Lou, Adv. Mater. 35 (2023) 2207888.
[63] J. Ding, D. Guo, N. Wang, H.-F. Wang, X. Yang, K. Shen, L. Chen, Y. Li, Angew. Chem. Int. Ed. 62 (2023) e202311909.
[64] Z. Sun, W. Xu, L. Guo, Q. Han, J. Gao, J. Wang, Y. Feng, C. Li, Q. Liang, H.-B. Sun, Y. Yang, J. Energy Chem. 70 (2022) 74–83.
[65] J. Yu, Y. Qian, S. Seo, Y. Liu, H.T.D. Bui, N. Quang Tran, J. Lee, A. Kumar, H. Wang, Y. Luo, X. Shao, Y. Cho, X. Liu, M. Gyu Kim, H. Lee, J. Energy Chem. 85 (2023) 11–18.
[66] W. Cheng, X.F. Lu, D. Luan, X.W. Lou, Angew. Chem. Int. Ed. 59 (2020) 18234–18239.
[67] R. Liu, M. Sun, X. Liu, Z. Lv, X. Yu, J. Wang, Y. Liu, L. Li, X. Feng, W. Yang, B. Huang, B. Wang, Angew. Chem. Int. Ed. 62 (2023) e202312644.
[68] R. Wang, J. Liu, J. Xie, Z. Cai, Y. Yu, Z. Zhang, X. Meng, C. Wang, X. Xu, J. Zou, Appl. Catal. B Environ. 324 (2023) 122230.